Presupernova Neutrinos

Realistic Emissivities from Stellar Evolution

Patton, K.M.; Lunardini, C.; Farmer, R.J.

DOI
10.3847/1538-4357/aa6ba8

Publication date
2017

Document Version
Final published version

Published in
Astrophysical Journal

The Astrophysical Journal, 840:2 (14pp), 2017 May 1 https://doi.org/10.3847/1538-4357/aa6ba8

Presupernova Neutrinos: Realistic Emissivities from Stellar Evolution

Kelly M. Patton[1,2], Cecilia Lunardini[1], and Robert J. Farmer[3]
[1] Department of Physics, Arizona State University, Tempe, AZ 85287-1504, USA; kmpatton@uw.edu, cecilia.lunardini@asu.edu
[2] Institute for Nuclear Theory, University of Washington, Seattle, WA 98195, USA
[3] School of Earth and Space Exploration, Arizona State University, Tempe, AZ 85287-1504, USA; rjfarmer@asu.edu
Received 2016 May 16; revised 2017 March 29; accepted 2017 April 3; published 2017 April 26

Abstract

We present a new calculation of neutrino emissivities and energy spectra from a massive star going through the advanced stages of nuclear burning (presupernova) in the months before becoming a supernova. The contributions from β decay and electron capture, pair annihilation, plasmon decay, and the photoneutrino process are modeled in detail, using updated tabulated nuclear rates. We also use realistic conditions of temperature, density, electron fraction, and nuclear isotopic composition of the star from the state-of-the-art stellar evolution code MESA. Results are presented for a set of progenitor stars with mass between 15 $M_\odot$ and 30 $M_\odot$. It is found that β processes contribute substantially to the neutrino emissivity above realistic detection thresholds of few MeV, at selected positions and times in the evolution of the star.

Key words: astroparticle physics – neutrinos

1. Introduction

A very luminous burst of neutrinos is the first signal that we receive—possibly together with gravitational waves—informing us that a star's core has collapsed, and that just a few hours afterwards the initially masked electromagnetic components will escape, becoming a supernova. Since their first (and only) detection in 1987 (Alekseev et al. 1987; Bionta et al. 1987; Hirata et al. 1987), neutrinos from stellar collapse have been studied in their rich phenomenology, including their role in the dynamics of collapse and explosion, the effects on nucleosynthesis processes in the stellar matter, and the complicated pattern of neutrino flavor oscillations inside the star and in the Earth (see, e.g., Mirizzi et al. 2016).

Interestingly, neutrinos can also offer a unique signature of the stages of stellar evolution that lead up to collapse ("presupernova"), on which still little is known, at least observationally, compared with the dramatic postcollapse events. As a massive star ($M \gtrsim 8\,M_\odot$, with $M_\odot$ the mass of the Sun) nears the end of its lifetime, the chain of nuclear burning in its core and inner shells proceeds through the fusion of progressively heavier elements. The central temperature and density of the star increase dramatically, resulting in an equally dramatic increase in the flux and average energies of neutrinos emitted. These neutrinos could become detectable months before the collapse, during the oxygen-burning phase, for the closest supernova candidate, Betelgeuse. Days or hours before (silicon-burning phase) might be more realistic for a star a few kiloparsecs away (Odrzywolek & Heger 2010; Asakura et al. 2016).

Although challenging, the observation of presupernova neutrinos would be extremely rewarding: it would offer an unprecedented direct probe of nuclear fusion beyond hydrogen and helium, and give us a firsthand narrative of the very late stages of stellar evolution in terms of density and temperature near the star's core. Considering the excellent timing resolution of current neutrino detectors, this narrative could be seen in real time, and would be a precious alert of the upcoming postcollapse neutrino burst and supernova.

Besides their detection, the production and propagation of presupernova neutrinos are important ingredients of models of stellar evolution. In the later stages of nuclear burning, neutrinos become the main source of energy loss, while also increasing the entropy of the star as it nears core collapse (Woosley et al. 2002). The physics of these neutrinos is interesting, also as an important application of the more general problem of neutrino emission in hot and dense stellar matter.

With these motivations, studies have been conducted on the neutrino emissivity of stars in the presupernova stage. Most of the literature so far has focused on neutrinos produced via thermal processes, for representative conditions (temperature, density, and chemical potential) of the stellar matter. The earliest works (Odrzywolek et al. 2004a, 2004b; Kutschera et al. 2009) included only the pair annihilation process, and parameters typical of the Si burning phase. The possibility to detect the resulting neutrino flux was discussed, with encouraging conclusions. A more detailed study of presupernova neutrinos from thermal processes, and their detectability, has appeared recently (Kato et al. 2015), including pair annihilation and plasmon decay. Rather than representative parameters, this work uses realistic, time-evolving profiles of temperature, density, and chemical potential from numerical models of stellar evolution (Takahashi et al. 2013). A second paper by a subset of the authors of Kato et al. (2015) explores in detail the pair annihilation neutrino spectra and detection potential in both current and future detectors, with emphasis on what the variation in the neutrino signal can indicate about stellar evolution (Yoshida et al. 2016).

Until now, the role of β processes in presupernova neutrinos has been discussed only in terms of the basics, in the works of Odrzywolek and Heger (Odrzywolek 2009; Odrzywolek & Heger 2010). Here, arguments of nuclear statistical equilibrium or α networks are used to determine isotopic composition. In Odrzywolek & Heger (2010), it is explicitly emphasized that both methods are inadequate, and that a full, self-consistent stellar evolution simulation, with a large and accurate nuclear reaction network, is ultimately needed.

In this work, such rigorous approach is realized for the first time. We present a new, comprehensive calculation of the presupernova neutrino emission, which includes, in addition to the main thermal processes (pair annihilation, plasmon decay, and the photoneutrino process), a detailed treatment of β decay

Table 1
Summary of the Processes Included in This Work, with the Main References to Prior Literature

	Processes	Formulae	Main References
Beta	$\beta^{\pm}$ decay	$A(N, Z) \rightarrow A(N-1, Z+1) + e^{-} + \overline{\nu}_e$	Fuller et al. (1980, 1982a, 1982b, 1985), Langanke & Martinez-Pinedo (2001), Oda et al. (1994), Odrzywolek (2009)
		$A(N, Z) \rightarrow A(N+1, Z-1) + e^{+} + \nu_e$	
	e^{+}/e^{-} capture	$A(N, Z) + e^{-} \rightarrow A(N+1, Z-1) + \nu_e$	
		$A(N, Z) + e^{+} \rightarrow A(N-1, Z+1) + \overline{\nu}_e$	
Thermal	Plasma	$\gamma^{*} \rightarrow \nu_{\alpha} + \overline{\nu}_{\alpha}$	Ratkovic et al. (2003), Odrzywolek (2007)
	Photoneutrino	$e^{\pm} + \gamma \rightarrow e^{\pm} + \nu_{\alpha} + \overline{\nu}_{\alpha}$	Dutta et al. (2004)
	Pair	$e^{+} + e^{-} \rightarrow \nu_{\alpha} + \overline{\nu}_{\alpha}$	Misiaszek et al. (2006)

and electron capture. These processes are modeled using updated nuclear rate tables (Oda et al. 1994; Langanke & Martinez-Pinedo 2001) as a supplement to the classic ones by Fuller, Fowler, and Newman (FFN; Fuller et al. 1980, 1982a, 1982b, 1985). The relevant microphysics is then applied to a realistic star using the detailed, time-evolving profiles of temperature, density, and nuclear isotopic composition from the state-of-the-art stellar evolution code MESA (Modules for Experiments in Stellar Astrophysics; Paxton et al. 2011, 2013, 2015). We place emphasis on modeling of the neutrino spectrum above a realistic detection threshold of 2 MeV; this requires including certain β processes that are subdominant in the total energy budget of the star.

The paper is structured as follows. After a summary of background information (Section 2), the relevant formalism of neutrino emissivities and spectra is discussed in Section 2.1 for β processes, and in Section 2.2 for thermal processes. In Section 3 numerical results are shown for several steps of a star's presupernova evolution, and for different progenitor stars, as modeled by MESA. A discussion and final considerations are given in Section 4.

2. Neutrino Production in a Presupernova Environment

About $\sim 10^3$ years before becoming a supernova, a star begins to experience the fusion of heavy (beyond helium) elements. First, carbon fusion is ignited; as the temperature and density increases, then the fusion of Ne, O, and Si take place in the core of the star. Each stage is faster than the previous one: the core O burning phase only lasts a few months, and the core Si burning only takes a few days (Woosley et al. 2002). Immediately before collapse, the star is characterized by a shell structure, with an iron core at the center, surrounded by shells where heavy element fusion is still taking place efficiently.

In the increasingly dense and hot environment of a presupernova, neutrinos are produced more and more abundantly through several processes, which we broadly categorize as β and thermal. Here the neutrino emissivities and spectra are calculated for the four main processes, using analytic and semi-analytic results from the literature, as summarized in Table 1. Each process is discussed in detail in the subsections that follow.

2.1. β Processes

When a star reaches the presupernova phase, its nuclear isotopic composition is complex and constantly changing. Therefore, to calculate the ν_e and $\bar{\nu}_e$ fluxes from β processes (Table 1) requires information on a vast array of nuclear transitions.

Here we use the rate tables compiled by FFN (Fuller et al. 1980, 1982a, 1982b, 1985), Oda et al. (OEA) (Oda et al. 1994), and Langanke and Martinez-Pinedo (LMP; Langanke & Martinez-Pinedo 2001). Each table uses shell model calculations, including experimental data when available, to find rates of electron (positron) capture and $\beta^{\pm}$ decays for a grid of temperature and density values, under the assumption that there is a strong contribution from Gamow–Teller (GT) transitions. The FFN table covers isotopes with $21 \leqslant A \leqslant 60$, while OEA covers $17 \leqslant A \leqslant 39$ and LMP is calculated for $45 \leqslant A \leqslant 65$. Where overlap between different tables occurs, precedence is given, in order, to LMP, and then OEA and finally FFN. This is the same convention used by MESA (Paxton et al. 2011).

Let us summarize the calculation of neutrino β emissivities and spectra. The rate of weak decay from the ith parent state to the jth daughter state is written as (Fuller et al. 1980)

$$\lambda_{ij} = \log 2 \frac{f_{ij}(T, \rho, \mu_e)}{\langle ft \rangle_{ij}}. \tag{1}$$

The quantity $\langle ft \rangle_{ij}$ is the comparative half-life for the process, and is related to the weak interaction matrix element. For the tables of FFN, OEA, and LMP, the value of $\langle ft \rangle$ is taken either from experimental measurements or from estimates of the strength of GT and Fermi transitions.

The function $f_{ij}(T, \rho, \mu_e)$ is the phase space integral for the process. The phase space of an outgoing electron with momentum p' is given by

$$dn_{p'} = p'^2 dp \left(1 - \frac{1}{1 + \exp((E_{e'} - \mu_e)/kT)}\right), \tag{2}$$

while for an incoming electron with momentum p it is

$$dn_p = p^2 dp \left(\frac{1}{1 + \exp((E_e - \mu_e)/kT)}\right). \tag{3}$$

Here, p and $E_e = \sqrt{p^2 + m_e^2}$ are the momentum and energy of the electron, μ_e is the chemical potential, and T is the temperature. As in Odrzywolek (2009), we define the chemical potential, including the rest mass, so that $\mu_{e^-} = -\mu_{e^+}$. The outgoing neutrinos are assumed to have no inhibition of the final state (Fuller et al. 1980), so the phase space factor is simply $E_\nu^2 dE_\nu$. In other words, while the incoming and outgoing electrons must conform to a Fermi–Dirac distribution, neutrinos have no such restriction.

For a given nuclear transition, the Q-value is defined as (Fuller et al. 1980)

$$Q_{ij} = M_p - M_d + E_i - E_j, \tag{4}$$

where M_p and E_i (M_d and E_j) are the mass and excitation energy of of the parent (daughter) nucleus. Since we are interested in the rate as a function of neutrino energy, we can rewrite the electron phase space integrals, Equations (2)–(3), in terms of the neutrino energy, E_ν, using energy conservation (i.e., $Q_{ij} = E_e + E_\nu$ for β decay, and $Q_{ij} + E_e = E_\nu$ for electron capture). These phase space integrals contain all of the dependence on neutrino energy, and thus solely determine the shape of the neutrino energy spectra.

Following the approach of Langanke et al. (2001), we adopt a single, effective Q-value, Q, for each isotope, and treat it as a fit parameter. This effective Q-value is found by requiring that the average neutrino energy matches the value obtained from the nuclear rate tables—that is,

$$\langle E_{\nu,\bar\nu}\rangle = \frac{\int_0^\infty (d\lambda/dE_\nu) E_\nu dE_\nu}{\int_0^\infty (d\lambda/dE_\nu) dE_\nu} = \frac{\mathcal{E}^{\nu,\bar\nu}}{\lambda^{\rm EC,PC} + \lambda^{\beta^\pm}}, \tag{5}$$

where the quantities on the right side of the equation are obtained from the rate tables. Here $\lambda^{\rm EC,PC}$ and $\lambda^{\beta^\pm}$ are the electron (positron) capture rate and $\beta^\pm$ decay rates (Langanke & Martinez-Pinedo 2001), $\lambda = \lambda^{\rm EC,PC} + \lambda^{\beta^\pm}$, and $\mathcal{E}^{\nu,\bar\nu}$ is the rate of energy loss as (anti-)neutrinos. Note that $\langle E_{\nu,\bar\nu}\rangle$ is a combined value, including both the capture and decay values weighted by the respective rates. Therefore, by construction, the Q-value found from Equation (5) is the same for both decay and capture. Here and throughout the paper, subscripts or superscripts such as in $\langle E_{\nu,\bar\nu}\rangle$ indicate that an equation is true for, in this example, $\langle E_\nu\rangle$ and $\langle E_{\bar\nu}\rangle$, with all subscripted values in the equation taking either ν or $\bar\nu$ as necessary.

Combining Equations (1)–(5), we find the spectra for the weak processes for a single isotope:

$$\phi_{\rm EC,PC} = N_{\rm EC,PC} \frac{E_\nu^2 (E_\nu - Q)^2}{1 + \exp((E_\nu - Q - \mu_e)/kT)} \Theta \times (E_\nu - Q - m_e) \tag{6}$$

$$\phi_\beta = N_\beta \frac{E_\nu^2 (Q - E_\nu)^2}{1 + \exp((E_\nu - Q + \mu_e)/kT)} \Theta(Q - m_e - E_\nu), \tag{7}$$

where N_i is a normalization factor defined such that

$$\lambda^i = \int_0^\infty \phi_i dE_\nu \quad i = \text{EC, PC, } \beta^\pm. \tag{8}$$

Let us note that the presupernova environment is different from that of a supernova. For a supernova, the high electron degeneracy inhibits β decay, so that electron capture plays a stronger role (Langanke et al. 2001; Sullivan et al. 2016); in our case of interest, instead, lower degeneracies allow β decays to proceed. Their importance has been emphasized in Aufderheide et al. (1994a, 1994b), Martinez-Pinedo et al. (2000), and Heger et al. (2001).

Finally, the total ν_e (or $\bar\nu_e$) spectrum is found by a weighted sum over all the isotopes present,

$$\Phi_{\nu,\bar\nu} = \sum_k \phi_k n_k = \sum_k X_k \phi_k \frac{\rho}{m_p A_k}, \tag{9}$$

where ρ is the mass density and m_p is the mass of the proton. Here ϕ_k is the sum of the normalized electron (positron) capture and $\beta^\pm$ decay spectra for isotope k; $n_k = X_k \rho/(m_p A_k)$ is the number density of the same isotope; and X_k, A_k are its mass fraction and atomic number, respectively (Odrzywolek 2009).

The values of X_k and ρ are taken from MESA calculations (Paxton et al. 2011, 2013, 2015). The features of the spectrum $\Phi_{\nu,\bar\nu}$ depend on the temperature, density, and isotopic abundances. For the center of a star immediately before collapse ($T \approx (4\text{–}5) \times 10^9$ K, $\rho \approx 10^7$ g cm^{-3}), the total spectrum can extend to several MeV.

2.2. Thermal Processes

Let us now discuss the three most important thermal processes: plasmon decay, photoneutrino production, and pair annihilation (Table 1). The total emissivities of all these processes, over a range of temperatures and densities, were discussed in detail by Itoh & Kohyama (1983), and Itoh et al. (1989, 1992, 1996a, 1996b). The differential rates and emissivities of selected process have been discussed by several authors (Ratkovic et al. 2003; Dutta et al. 2004; Misiaszek et al. 2006; Odrzywolek 2007; Kato et al. 2015; Asakura et al. 2016). In this section, we summarize the formalism relevant to our calculation.

2.2.1. Plasma Neutrino Process

In the plasma neutrino process, an excitation in the plasma (plasmon) decays into a neutrino–antineutrino pair. As shown in Itoh et al. (1996b), plasma neutrinos dominate the total emissivity at high densities. Detailed derivations and discussions of this process are given in Ratkovic et al. (2003) and Odrzywolek (2007). Drawing from this literature, here the essential equations for calculating the plasmon decay neutrino spectrum are summarized.

The total rate R and emissivity Q are given by the integrals (Ratkovic et al. 2003)

$$R = \sum_\epsilon \int \frac{d^3k}{2\omega(2\pi)^3} Z(k) \frac{d^3q_1}{2\mathcal{E}_1(2\pi)^3} \frac{d^3q_2}{2\mathcal{E}_2(2\pi)^3} \times [\langle|\mathcal{M}|^2\rangle f_{\gamma^*}(\omega)(2\pi)^4 \delta^4(K - Q_1 - Q_2)] \tag{10}$$

$$Q = \sum_\epsilon \int \frac{d^3k}{2\omega(2\pi)^3} Z(k) \frac{d^3q_1}{2\mathcal{E}_1(2\pi)^3} \frac{d^3q_2}{2\mathcal{E}_2(2\pi)^3} \times [(\mathcal{E}_1 + \mathcal{E}_2)\langle|\mathcal{M}|^2\rangle f_{\gamma^*}(\omega)(2\pi)^4 \delta^4(K - Q_1 - Q_2)], \tag{11}$$

where $Q_{1,2} = (\mathcal{E}_{1,2}, \boldsymbol{q}_{1,2})$ are the four momenta of the daughter neutrino pair, and $K = (\omega, \boldsymbol{k})$ and f_{γ^*} are the plasmon four momentum and spectrum:

$$f_{\gamma^*} = \frac{1}{e^{\omega_{T,L}/kT} - 1}. \tag{12}$$

The factor $Z(k)$ in Equations (10) and (11) is the residue from integrating around the pole in the propagator. The sums in Equations (10) and (11) are over the polarizations appropriate

for the decay mode. There are two possible decay modes: transverse (T), which has two polarizations, and longitudinal (L), with one polarization.

The term $\langle|\mathcal{M}|^2\rangle$ is the squared matrix element for the process. The effective vertex for plasmon decay has both vector and axial vector pieces (Braaten & Segel 1993). For the longitudinal decay mode, the axial vector term disappears, leaving the squared matrix element as (Ratkovic et al. 2003)

$$\langle|\mathcal{M}|^2\rangle^L = 2\frac{G_F^2(C_V^f)^2}{\pi\alpha}\left(\frac{\omega_L^2-k^2}{k^2}\right)^2\Pi_L^2(\omega_L,k) \times\left[\frac{(\mathcal{E}_1\omega_L-\boldsymbol{q}_1\cdot\boldsymbol{k})(\mathcal{E}_2\omega_L-\boldsymbol{q}_2\cdot\boldsymbol{k})}{\omega_L^2-k^2} + \frac{(\boldsymbol{k}\cdot\boldsymbol{q}_1)(\boldsymbol{k}\cdot\boldsymbol{q}_2)}{k^2}-\frac{\mathcal{E}_1\mathcal{E}_2+\boldsymbol{q}_1\cdot\boldsymbol{q}_2}{2}\right]. \quad (13)$$

On the other hand, both vector and axial vector pieces survive in the calculation of the transverse decay mode. After squaring, we are left with a transverse vector term proportional to $(C_V^f)^2$, an axial term with coefficient $(C_A^f)^2$, and a mixed term with a factor $(C_A^f C_V^f)$ (Ratkovic et al. 2003). Put together, the squared matrix element for the transverse decay mode is

$$\langle|\mathcal{M}|^2\rangle^T = \frac{G_F^2}{\pi\alpha}[((C_V^f)^2\Pi_T^2(\omega_T,k)+(C_A^f)^2\Pi_A^2(\omega_T,k)) \times\left(\mathcal{E}_1\mathcal{E}_2-\frac{(\boldsymbol{k}\cdot\boldsymbol{q}_1)(\boldsymbol{k}\cdot\boldsymbol{q}_2)}{2}\right) + 2(C_A^f C_V^f)\frac{\Pi_A(\omega_T,k)\Pi_T(\omega_T,k)}{k} \times(\mathcal{E}_1(\boldsymbol{k}\cdot\boldsymbol{q}_2)-\mathcal{E}_2(\boldsymbol{k}\cdot\boldsymbol{q}_1))]. \quad (14)$$

The functions $\Pi_{L,T,A}$ are the longitudinal, transverse, and axial polarization functions, which are defined in (Ratkovic et al. 2003). The total emissivity for the plasmon decay process is found by summing all of these channels. The vector and axial couplings, C_V^f and C_A^f, are

$$\begin{aligned} C_V^e &= \frac{1}{2}+2\sin^2(\theta_W)\\ C_A^e &= \frac{1}{2}\\ C_V^x &= C_V^e-1\\ C_A^x &= C_A-1, \end{aligned} \quad (15)$$

with $\sin^2(\theta_W)=0.226$. The difference in these couplings results in a suppression of the ν_x flavors by factors of $(C_V^x/C_V^e)^2\approx 3\times10^{-3}$ (Odrzywolek 2007).

After integrating Equations (10) and (11) over the plasmon momentum and the angle between the outgoing neutrinos, one gets the rate, differential in the neutrino energy $\mathcal{E}_1$ (Odrzywolek 2007),

$$\frac{dR^{L,T}}{d\mathcal{E}_1}=\int_0^\infty d\mathcal{E}_2\frac{g_{L,T}}{\pi^4}Z_{L,T}\langle|\mathcal{M}|^2\rangle^{L,T}f_{\gamma^*}J_{L,T}S\,, \quad (16)$$

with $g_T=2$ and $g_L=1$ accounting for the number of polarizations for each mode. The new factor $J_{L,T}$ is the Jacobean resulting from the δ function integration. The factor S, is a product of step functions, describing the physically relevant region,

$$S=\Theta(4\mathcal{E}_1\mathcal{E}_2-m_{L,T}^2)\Theta(\mathcal{E}_1+\mathcal{E}_2-\omega_{L,T})\Theta \times(\omega_{\max}-\mathcal{E}_1-\mathcal{E}_2). \quad (17)$$

The maximum plasmon energy, $\omega_{\max}$, is finite for longitudinal plasmons, and depends on the temperature and density of the environment. Instead, $\omega_{\max}\to\infty$ for transverse plasmons. We have used the Braaten–Segel approximations (Braaten & Segel 1993) in all of these calculations, allowing the differential rate to be calculated analytically. The expressions for various plasma parameters, such as $\omega_{\max}$, $Z_{L,T}$, $\Pi_{L,T,A}$, and $J_{L,T}$ in this approximation, are given in Ratkovic et al. (2003) and Odrzywolek (2007). The total emissivity calculated through this method is consistent with the Itoh et al. formula for the plasma process.

The spectra of neutrinos from plasmon decay are typically colder that those from other processes (see Figures 3–6). The neutrinos resulting from longitudinal plasmon decay are limited by $\omega_{\max}$, with $\omega_{\max}<$ MeV for typical presupernova temperatures and densities. Neutrinos from transverse plasmon decay have no such energy restriction, however, and can extend beyond 1 MeV in some cases. In all likelihood, the plasmon decay contribution cannot be individually identified in a detector; nevertheless, it can have a major impact on the total neutrino emissivity at some points in the lifetime of the star.

2.2.2. Photoneutrino Process

For the photoneutrino process, we follow the extensive discussion in Dutta et al. (2004). The calculation of rates and emissivities is very similar to that for the plasma neutrino process. In this case, the total rate R and emissivity Q are calculated by performing the integrals

$$R=\int\frac{2d^3p}{(2\pi)^3}\frac{f_e(E_P)}{2E_P}\int\frac{\xi d^3k}{(2\pi)^3}\frac{f_\gamma(\omega)}{2\omega} \times\int\frac{d^3p'}{(2\pi)^3}\frac{1-f_e(E_{P'})}{2E_{P'}}\int\frac{d^3q_1}{(2\pi)^3}\frac{1}{2\mathcal{E}_1} \times\int\frac{d^3q_2}{(2\pi)^3}\frac{1}{2\mathcal{E}_2}(2\pi)^4\delta^4(P+K-P'-Q_1-Q_2) \times\frac{1}{\zeta}\langle|\mathcal{M}|^2\rangle \quad (18)$$

$$Q=\int\frac{2d^3p}{(2\pi)^3}\frac{f_e(E_P)}{2E_P}\int\frac{\xi d^3k}{(2\pi)^3}\frac{f_\gamma(\omega)}{2\omega} \times\int\frac{d^3p'}{(2\pi)^3}\frac{1-f_e(E_{P'})}{2E_{P'}}\int\frac{d^3q_1}{(2\pi)^3}\frac{1}{2\mathcal{E}_1} \times\int\frac{d^3q_2}{(2\pi)^3}\frac{1}{2\mathcal{E}_2}(2\pi)^4\delta^4(P+K-P'-Q_1-Q_2) \times(\mathcal{E}_1+\mathcal{E}_2)\frac{1}{\zeta}\langle|\mathcal{M}|^2\rangle. \quad (19)$$

As in Equations (10) and (11), these expressions are integrals of the squared matrix element over the incoming and outgoing momenta, taking into account the photon and electron distributions and energy conservation. Here, $P=(E_P,\boldsymbol{p}_{1,2})$ is the four momentum for the incoming electron and $P'=(E_{P'},\boldsymbol{p}')$

is the same for the outgoing electron. Following the notation defined in the plasma neutrino discussion, $Q_{1,2} = (\mathcal{E}_{1,2}, \boldsymbol{q}_{1,2})$ are the four momenta for the outgoing neutrino pair and $K = (\omega, \boldsymbol{k})$ is the four momentum of the photon.

The sums run over the polarization of the photon and spin of the incoming and outgoing electrons. Here, the initial factor of two accounts for the spin of the incoming electron, ξ is due to the polarization of the incoming photon, and ζ is from the spins of the outgoing electron and neutrinos. Similar to plasmon decay, there are transverse and longitudinal modes for the photoneutrino process. For the transverse mode of the photon, $\xi = 2$ and $\zeta = 4$. In the longitudinal case, $\xi = 1$ and $\zeta = 2$ (Dutta et al. 2004).

As discussed in Dutta et al. (2004), the squared matrix element can be derived to be

$$\langle|\mathcal{M}|^2\rangle^{T(L)} = 32e^2G_F^2[((C_V^f)^2 - (C_A^f)^2)m_e^2\mathcal{M}_-^{T(L)} + ((C_V^f)^2 + (C_A^f)^2)\mathcal{M}_+^{T(L)} + C_V^f C_A^f \mathcal{M}_\times^{T(L)}]. \quad (20)$$

This simple form includes the terms $\mathcal{M}_-$, $\mathcal{M}_+$, and $\mathcal{M}_\times$. These terms are complicated combinations of products of the four momenta and photon polarizations. The full expressions can be found in the Appendix A of Dutta et al. (2004).

The delta function in Equations (18) and (19) can be used to complete the integration over the incoming electron momentum $\boldsymbol{p}$ and the incoming photon angle θ_k. As in Dutta et al. (2004), here the coordinate system is such that one neutrino momentum is aligned with the z-axis, with the second neutrino momentum in the x–z plane at an angle $\theta_{q_1q_2}$, while the outgoing electron momentum $\boldsymbol{p}'$ is in an arbitrary direction defined by angles θ_e and ϕ_e. In this formalism, we can find the total four momentum of the system, $P_{\rm tot} = P + K = P' + Q_1 + Q_2$, and thus determine the momenta of the incoming photon and electron. For details on these initial integrations, see Dutta et al. (2004).

The result for the differential rates and emissivities is the following:

$$\frac{dR}{d\mathcal{E}_1} = \frac{\pi^2}{(2\pi)^9}\mathcal{E}_1\int_0^\infty \mathcal{E}_2 d\mathcal{E}_2 \int_{-1}^1 d\cos\theta_{q_1q_2} \times \int_0^\infty \frac{|\boldsymbol{p}'|^2}{E_{P'}} d|\boldsymbol{p}'| \int_{-1}^1 d\cos\theta_e \times \int_0^{2\pi} d\phi_e [1 - f_e(E_{P'})] I(p', q_1, q_2) \quad (21)$$

$$\frac{dQ}{d\mathcal{E}_1} = \frac{\pi^2}{(2\pi)^9}\mathcal{E}_1\int_0^\infty \mathcal{E}_2 d\mathcal{E}_2 \int_{-1}^1 d\cos\theta_{q_1q_2} \times \int_0^\infty \frac{|\boldsymbol{p}'|^2}{E_{p'}} d|\boldsymbol{p}'| \int_{-1}^1 d\cos\theta_e \times \int_0^{2\pi} d\phi_e [1 - f_e(E_{P'})] \times (\mathcal{E}_1 + \mathcal{E}_2) I(p', q_1, q_2), \quad (22)$$

where the integral $I(p', q_1, q_2)$ is defined as

$$I(p', q_1, q_2) = \frac{1}{2\pi^2}\int_0^\infty \frac{|\boldsymbol{k}|}{\omega} d|\boldsymbol{k}| \int_0^{2\pi} d\phi_k \times \left[f_\gamma(\omega) f_e(E_P) \frac{1}{|\boldsymbol{P}_{\rm tot}|}\langle|\mathcal{M}|^2\rangle^{T(L)}\right]. \quad (23)$$

The seven-dimensional integrals in Equations (21)–(22) are calculated by a Monte Carlo method, as in Dutta et al. (2004). As with the plasma process, our calculation using the methods of Dutta et al. (2004) is consistent with the formula from Itoh et al. (1996a).

As will be shown in Section 3, photoneutrinos dominate the total emissivity at a few locations in the outer shells of the star, in agreement with the results in Itoh et al. (1996a). However, for the part of the presupernova neutrino flux that is of most interest for detection—corresponding to higher temperatures and densities—these neutrinos are typically overwhelmed by pair and β process neutrinos.

2.2.3. Pair Annihilation Neutrinos

The emissivity for neutrinos from pair annihilation, $e^+ + e^- \rightarrow \nu + \overline{\nu}$, can be calculated similarly to Equations (10) and (11): the squared matrix element for this process has to be integrated over the incoming and outgoing momenta, including considerations for the electron and positron momentum distributions and energy conservation. For the pair annihilation process, the expressions for the total rate R and emissivity Q are

$$R = \frac{4}{(2\pi)^8}\int \frac{d^3p_1}{2E_1} f_1(E_1) \int \frac{d^3p_2}{2E_2} f_2(E_2) \int \frac{d^3q_1}{2\mathcal{E}_1} \int \frac{d^3q_2}{2\mathcal{E}_2} \times [2\langle|\mathcal{M}|^2\rangle \delta^4(P_1 + P_2 - Q_1 - Q_2)], \quad (24)$$

$$Q = \frac{4}{(2\pi)^8}\int \frac{d^3p_1}{2E_1} f_1(E_1) \int \frac{d^3p_2}{2E_2} f_2(E_2) \int \frac{d^3q_1}{2\mathcal{E}_1} \int \frac{d^3q_2}{2\mathcal{E}_2} \times [(\mathcal{E}_1 + \mathcal{E}_2)\langle|\mathcal{M}|^2\rangle \delta^4(P_1 + P_2 - Q_1 - Q_2)], \quad (25)$$

where the squared matrix element, appropriately averaged over spin, is

$$\langle|\mathcal{M}|^2\rangle = 8G_F^2((C_A^f - C_V^f)^2(P_1 \cdot Q_1)(P_2 \cdot Q_2) + (C_A^f + C_V^f)^2(P_2 \cdot Q_1)(P_1 \cdot Q_2) + m_e^2(C_V^2 - C_A^2)(Q_1 \cdot Q_1)), \quad (26)$$

where $P_{1,2} = (E_{1,2}, \boldsymbol{p}_{1,2})$ are the four momenta of the incoming electron and positron, and $Q_{1,2} = (\mathcal{E}_{1,2}, \boldsymbol{q}_{1,2})$ are the four momenta of the outgoing neutrino and antineutrino. The functions $f_i(E_i)$ are the Fermi–Dirac distributions for the electron and positron.

As in the previous derivations for plasmon decay and the photoneutrino process, the delta function can be used to simplify the integral. Extensive algebra, an example of which can be found in Hannestad & Madsen (1994), reduces the calculation of the differential rate to a three-dimensional integral over the magnitudes of the electron and positron momenta and the angle between them,

$$\frac{dR}{d\mathcal{E}_i} = \int d^3p_1 d^3p_2 \frac{d\sigma\upsilon}{d\mathcal{E}_i} f_1 f_2, \quad (27)$$

where

$$d\sigma\upsilon = \frac{1}{2E_1}\frac{1}{2E_2}\frac{1}{(2\pi)^2}\delta^4(P_1 + P_2 - Q_1 - Q_2) \times \frac{d^3q_1}{2\mathcal{E}_1}\frac{d^3q_2}{2\mathcal{E}_2}\langle|\mathcal{M}|^2\rangle, \quad (28)$$

and υ being the relative velocity of the electron–positron pair. We have performed this integral using Monte Carlo integration.

In agreement with the results of Itoh et al. (1996a), the results of MESA show (Section 3) that pair neutrinos are the major contributors to the neutrino flux from the center of the star where temperatures and densities are highest. The energies of these neutrinos can reach up to several MeV, and along with the β process, produce most of the potentially detectable neutrinos.

3. Results: Neutrino Emission in an Evolving Star

3.1. The Calculation: Technical Aspects, Inputs, and Outputs

We employed the stellar evolution code MESA, version r7624 (Paxton et al. 2011, 2013, 2015), to simulate the evolution of progenitor stars with masses $M = 15, 20, 25, 30\,M_{\odot}$, from pre-main-sequence (pre-MS) to the onset of core collapse, which is defined as when the infall velocity anywhere in the star exceeds $V_{\rm max} = 1 \times 10^8\,{\rm cm\,s^{-1}}$. This final instant is defined as $t = t_c = 0$, and all the earlier times t ($t < 0$) will be defined relative to it, so that $-t > 0$ will indicate the time to collapse. The progenitor models used here are single, non-rotating, non-mass losing stars, with a solar metallicity (i.e., mass fraction $Z = 0.02$ of elements heavier than He) and a solar abundance distribution from Grevesse & Sauval (1998); see Farmer et al. (2016) for more details. Note that the range of masses we consider covers some of the diversity expected in the final outcome of the collapse: while the progenitors with lower mass are likely to generate a strong shockwave, resulting in a robust supernova explosion, the heavier ones ($M = 25, 30\,M_{\odot}$) were found to be candidates for direct black hole formation (without explosion, a "failed supernova"), due to their greater compactness (see, e.g., O'Connor and Ott 2011; Pejcha & Thompson 2015).

The MESA simulation includes the effects of semiconvection, convective overshooting, and thermohaline mixing. We use the models from Farmer et al. (2016) with $\Delta M_{\rm max} = 0.1$, where $\Delta M_{\rm max}$ specifies the maximum cell mass, and MESA's $\delta_{\rm mesh} = 1.0$, where $\delta_{\rm mesh}$ controls the relative variance between cells. The combination of these two settings results in ≈1000–2000 spatial zones at core collapse. The isotopic composition of the star was modeled using MESA's `mesa_204.net` reaction network, which includes 204 isotopes up to ^{66}Zn, including all relevant reactions, fully coupled to the hydrodynamics from the pre-MS to core collapse. The MESA inlists and stellar models are publicly available.[4]

For each time step of the evolution, MESA produces in output the temperature, mass density, proton fraction, electron degeneracy, and isotopic composition as a function of the radial coordinate. Using formulae from Itoh & Kohyama (1983), Itoh et al. (1989, 1992, 1996a, 1996b), MESA also calculates, and provides in output, the neutrino energy emissivity Q (i.e., the total energy emitted in neutrinos per unit volume per unit time) for each production channel in Table 1. This quantity was useful as a consistency check for the semi-analytical formalism in Section 2, which reproduces it correctly. The same formalism was then used to perform a separate calculation (which uses the thermodynamical quantities calculated in MESA, but is not embedded in it) of the neutrino energy spectra for each of the production channels.

[4] http://mesastar.org

To emphasize the part of the neutrino flux that is potentially detectable, from the neutrino spectra we derived a partial energy emissivity, $Q_{\rm th}$, defined as the energy emitted in neutrinos with energy $E > E_{\rm th}$ per unit volume per unit time, with $E_{\rm th} = 2\,{\rm MeV}$ being an indicative threshold for detectability. This is a realistic value for liquid scintillator detectors (e.g., An et al. 2016); the threshold is typically higher than ∼5 MeV at liquid argon and water Cherenkov experiments (Abe et al. 2011; Bishai et al. 2015).

The following subsections illustrate our results in graphics and text. The reader is referred to Table 2 for the complete numerical details.

3.2. A Neutrino History: Emissivity Profiles

Let us first trace the time evolution of a star in the presupernova phase in terms of neutrino emission. We focus on the electron neutrino species, and do not include neutrino flavor oscillations. The μ and τ flavors (collectively denoted ν_x here) only give subdominant contributions to rates and emissivities, because they are not produced in β processes and are suppressed in thermal processes. The μ and τ flavors are included in the total emissivities, but their spectra are not shown in Figures 3–6.

It is known (see, e.g., Weaver et al. 1978) that the rate of evolution, and in particular the duration of each stage of nuclear burning, depends strongly on the progenitor mass, with more massive stars evolving more rapidly. For this reason, to facilitate comparisons between runs with different progenitors, for each star model, results have been generated at five selected times, t_n ($n = 1, \ldots, 5$; see Table 2), which were chosen to correspond to a physical event or phase in the evolution: at t_1, the star's core is at the beginning of the O burning phase; t_2 is approximately central though the core Si burning phase; and t_3 marks the end of it. We set t_5 to be the last step of the evolution, corresponding to the onset of collapse: $t_5 = t_c$. At t_5, Si burning is occurring in an outer shell, around $\log(R/R_{\odot}) \approx -2.5$.

As expected, the t_n are very different for the different progenitor models: for $M = 15\,M_{\odot}$, we find $t_1 \simeq -1.4 \times 10^4$ hr (i.e., about 600 days before collapse), while for $M = 30\,M_{\odot}$, we have $t_1 \simeq -1.0 \times 10^3$ hr (∼44 days). Likewise, we find $t_3 \simeq -7.4$ hr for the $M = 15\,M_{\odot}$ and $t_3 = -0.97$ hr, for the $M = 30\,M_{\odot}$ star, thus confirming the faster evolution of more massive progenitors.

As an exception, the time t_4 ($t_3 < t_4 < t_5$) has been specifically set to be the same ($t_4 \sim -0.5$ hr) for all stars, so to offer guidance on how strongly an observed presupernova neutrino time profile might depend on the progenitor mass.

Figure 1 shows the radial distribution of Q and $Q_{\rm th}$ at each of the selected times, and for each progenitor model. At all times, Q is maximum in the region $R \lesssim 10^{-2.5}\,R_{\odot}$, and declines roughly as R^{-6} for larger radii. $Q_{\rm th}$ is within an order of magnitude or so of Q in the central region, and falls more steeply than Q with increasing radius. We note sharp, time-dependent discontinuities in the emissivities, which reflect the shell structure of the star. Figure 1 also shows the radial profiles of the electron degeneracy parameter, $\eta_e = \mu_e/T$. It appears clearly that η_e increases strongly over time in the star's core, rising from $\eta_e \sim 0$ to values as high as $\eta_e \simeq 11$ at $t = t_5$. As a consequence, ν_e production through β^- decays becomes increasingly inefficient due to electron Pauli blocking (see Section 3.3).

When comparing results for different stellar progenitors (Figure 1, Table 2), it appears that differences in the

Table 2
Selected Points in the Evolution of the Star

Time (hr)	$Q_{\rm int}$ (MeV s^{-1})	Stage	Point	$\log(T/K)$	$\log(\rho/{\rm g\ cm^{-3}})$	Y_e	η_e	$\log(R/R_\odot)$	Q (MeV cm^{-3} s^{-1})	$Q_{\rm th}$ (MeV cm^{-3} s^{-1})
				$15\,M_\odot$						
$t_1 = -14425.2$	3.499×10^{48}	Begin core O burning	(c1)	9.266	6.874	0.498	2.069	−4.118	1.2081×10^{23}	1.8006×10^{22}
$t_2 = -24.1$	9.276×10^{50}	Core Si burning	(s2)	9.268	6.712	0.493	1.449	−2.315	1.215×10^{23}	2.211×10^{21}
			(c2)	9.544	7.718	0.471	2.895	−4.560	1.347×10^{26}	5.398×10^{25}
$t_3 = -7.445$	3.212×10^{51}	End core Si burning	(c3)	9.594	8.197	0.458	4.489	−4.560	2.501×10^{26}	1.325×10^{26}
$t_4 = -0.479$	1.708×10^{52}	1/2 hr pre-collapse	(c4)	9.658	8.769	0.445	6.815	−4.750	1.787×10^{27}	9.577×10^{26}
$t_5 = t_c$	1.749×10^{55}	Begin collapse	(c5)	9.929	9.969	0.432	10.188	−4.150	1.834×10^{32}	1.696×10^{32}
				$20\,M_\odot$						
Time (hr)	$Q_{\rm int}$ (MeV s^{-1})	Stage	Point	$\log(T/K)$	$\log(\rho/{\rm g\ cm^{-3}})$	Y_e	η_e	$\log(R/R_\odot)$	Q (MeV cm^{-3} s^{-1})	$Q_{\rm th}$ (MeV cm^{-3} s^{-1})
$t_1 = -2596.2$	2.479×10^{49}	Begin core O burning	(c1)	9.292	6.626	0.498	1.009	−3.994	3.006×10^{23}	3.560×10^{22}
$t_2 = -24.52$	1.645×10^{51}	Core Si burning	(s2)	9.319	6.753	0.494	1.239	−2.307	5.186×10^{23}	1.886×10^{22}
			(c2)	9.539	7.661	0.488	2.770	−4.339	1.261×10^{26}	5.309×10^{25}
$t_3 = -11.507$	2.647×10^{51}	End core Si burning	(c3)	9.561	7.586	0.481	2.256	−4.314	2.376×10^{26}	1.079×10^{26}
$t_4 = -0.465$	4.281×10^{52}	1/2 hr pre-collapse	(c4)	9.690	8.552	0.450	5.037	−4.636	3.471×10^{27}	2.265×10^{27}
$t_5 = t_c$	1.343×10^{55}	Begin collapse	(c5)	9.945	9.728	0.437	7.998	−4.028	6.761×10^{31}	6.348×10^{31}
				$25\,M_\odot$						
Time (hr)	$Q_{\rm int}$ (MeV s^{-1})	Stage	Point	$\log(T/K)$	$\log(\rho/{\rm g\ cm^{-3}})$	Y_e	η_e	$\log(R/R_\odot)$	Q (MeV cm^{-3} s^{-1})	$Q_{\rm th}$ (MeV cm^{-3} s^{-1})
$t_1 = -1402.2$	6.345×10^{49}	Begin core O burning	(c1)	9.306	6.537	0.498	0.652	−3.932	4.543×10^{23}	5.642×10^{22}
$t_2 = -23.79$	2.133×10^{51}	Core Si burning	(c2)	9.545	7.636	0.481	0.870	−4.229	4.174×10^{22}	3.542×10^{20}
			(s2)	9.545	7.636	0.481	2.594	−4.229	1.449×10^{26}	5.883×10^{25}
$t_3 = -11.81$	6.164×10^{51}	End core Si burning	(c3)	9.591	7.890	0.463	3.112	−4.383	3.052×10^{26}	1.418×10^{26}
$t_4 = -0.536$	1.695×10^{52}	1/2 hr pre-collapse	(c4)	9.684	8.851	0.443	6.886	−4.804	6.527×10^{27}	4.021×10^{27}
$t_5 = t_c$	1.921×10^{55}	Begin collapse	(c5)	9.934	10.078	0.428	11.046	−5.112	3.227×10^{32}	2.979×10^{32}
				$30\,M_\odot$						
Time (hr)	$Q_{\rm int}$ (MeV s^{-1})	Stage	Point	$\log(T/K)$	$\log(\rho/{\rm g\ cm^{-3}})$	Y_e	η_e	$\log(R/R_\odot)$	Q (MeV cm^{-3} s^{-1})	$Q_{\rm th}$ (MeV cm^{-3} s^{-1})
$t_1 = -1063.2$	7.100×10^{49}	Begin core O burning	(c1)	9.307	6.532	0.498	0.627	−3.904	4.713×10^{23}	5.552×10^{22}
$t_2 = -12.04$	5.056×10^{51}	Core Si burning	(s2)	9.295	6.428	0.499	0.395	−2.211	3.085×10^{23}	7.273×10^{21}
			(c2)	9.550	7.612	0.490	2.481	−4.264	7.867×10^{25}	5.705×10^{25}
$t_3 = -0.965$	9.430×10^{51}	End core Si burning	(c3)	9.579	7.521	0.481	1.872	−4.233	4.180×10^{26}	2.090×10^{26}
$t_4 = -0.509$	1.156×10^{53}	1/2 hr pre-collapse	(c4)	9.734	8.547	0.449	4.427	−4.576	9.103×10^{27}	6.551×10^{27}
$t_5 = t_c$	1.953×10^{55}	Begin collapse	(c5)	9.972	9.694	0.437	7.249	−4.958	1.176×10^{32}	1.138×10^{32}

Note. The first two columns give the instants of time (with $t = 0$ the time of collapse; see text) and the volume-integrated neutrino emissivity at these times. The following columns refer to specific points inside the star, for which the neutrino spectra were calculated. All points are at the core of the star. Column 3 specifies the evolutionary stage of the star. For each set of point and time, Columns 5–11 specify the temperature, density, electron fraction, electron degeneracy, radial coordinate, and neutrino emissivity (total of all flavors) Q and $Q_{\rm th}$.

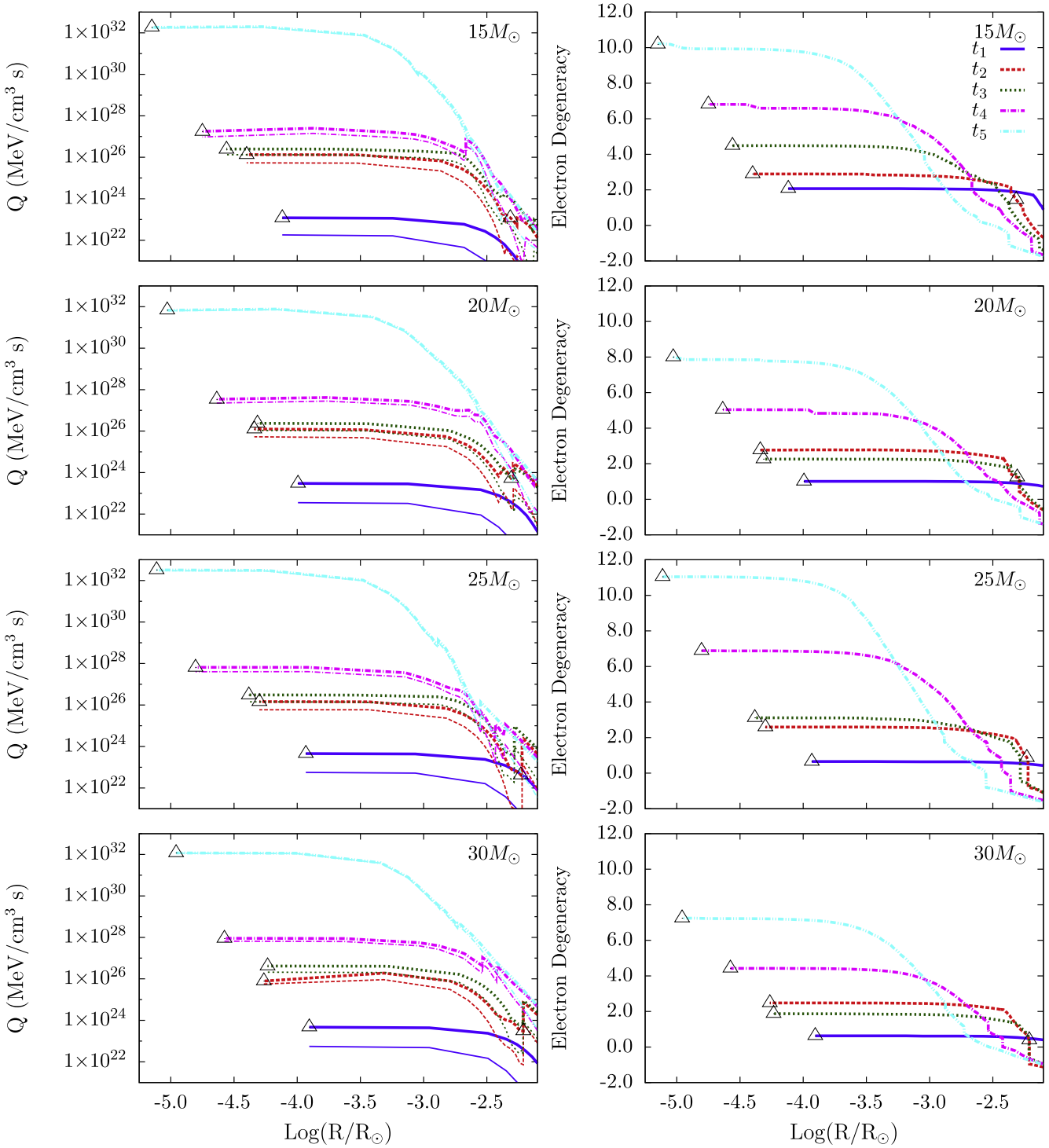

Figure 1. Left: the total neutrino emissivity in the star, Q (thick lines), and the emissivity for $E > 2$ MeV, $Q_{\rm th}$ (thin lines), as functions of the radial coordinate, for each progenitor star, and for the selected times in Table 2. Right: the radial profiles of the electron degeneracy parameter, $\eta_e = \mu_e/T$, for the same progenitors and times. In all figures, sample points are marked; details about them are given in Table 2 and Figures 3–6.

emissivities are larger at early times, and become more modest at later times, with the more massive stars generally having larger neutrino emissivities. For example, the emissivity integrated over the volume of the star, $Q_{\rm int}$, at time t_1, is a factor of ∼20 larger for the $M = 30\ M_\odot$ star than for the $15\ M_\odot$ one, but at $t = t_5$, differences in $Q_{\rm int}$ are at the level of tens of percent only. The local emissivities Q at selected radii inside the star show a similar trend (Table 2); however, differences between progenitors are more modest, at the level of a factor of ∼2–3. At the fixed time t_4 (half hour before collapse), differences are substantial, about an order of magnitude in $Q_{\rm int}$ and a factor ∼4 in Q in the core, between the least and the most massive progenitors, thus suggesting the possibility to use the time profile of a neutrino signal in a detector for progenitor

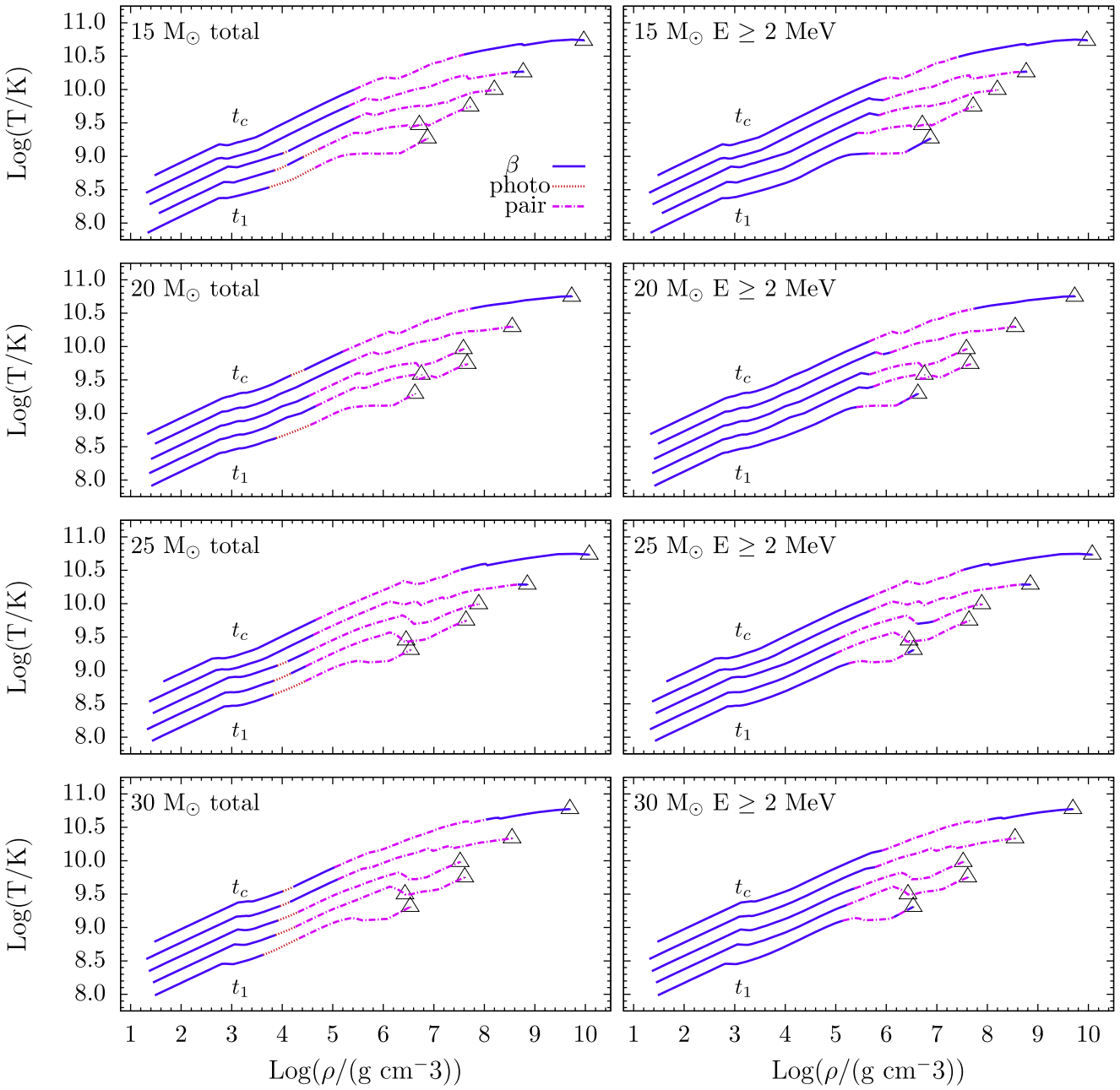

Figure 2. Left: origin of the dominant neutrino emissivity as calculated by MESA as a function of both temperature and density, for the same time instants t_n, as in Figure 1 ($n = 1, 5$, from bottom to top). Each curve describes the temperature and density encountered at different radii within the star at a given time t. The different dashes/colors indicate which process dominates the total emissivity (see legend). For better visibility, the curve for the time t_n is shifted upward vertically by $0.2(n-1)$ units. The selected points in Table 2 are marked. Right: the same figure, but for the emissivity of potentially detectable neutrinos (with energy $E \geqslant 2$ MeV).

identification. The dependence on the progenitor mass/model found here is overall consistent with the faster evolution of the more massive progenitors. The electron degeneracy, η_e, only varies mildly between progenitors, by tens of percent.

We note that variations are not always monotonic with the progenitor mass; for example, the $M = 20\,M_\odot$ star has the largest emissivity and the largest η_e in the core (Figure 1). This non-monotonic behavior reflects the underlying non-monotonic character of the stellar models themselves and the non-linear nature of stellar evolution. As a star evolves off of the the giant branch, forming a carbon/oxygen core, the degeneracy of the core begins to play a larger role in the stars' evolution. The relevant timescales are set by an interplay of the neutrino losses and the ignition of each subsequent fuel source. A star may ignite one or more off-center shell flashes while burning oxygen or silicon in its core. If the energy released by the ignition is much greater than the local neutrino cooling rate, then the shell flash may drive a convection zone, which can mix in fresh fuel, keeping the shell burning. This can lead to discontinuous changes (with respect to changes in the initial mass) between models that do and do not drive a convection zone (Heger et al. 2001). This complex interplay between the type of ignitions, formation, and size of convection zones, and the composition of the material post ignition, can lead to non-linear behavior of the star with respect to increasing initial mass. For instance, at $\approx 20\,M_\odot$ there is a complex transition

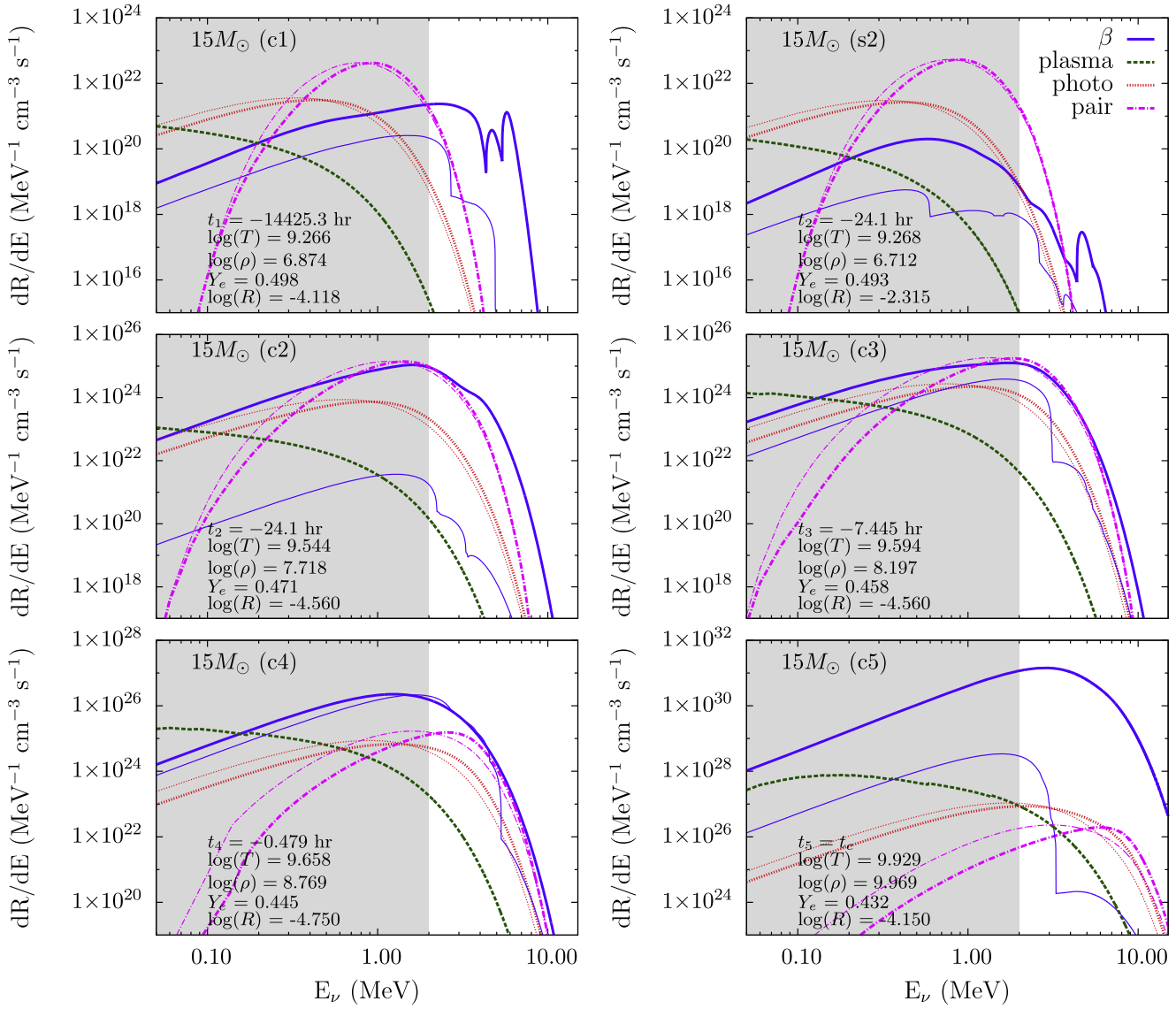

Figure 3. Neutrino spectra for different processes, for the 15 $M_\odot$ star, for the points (c1)–(c5) and (s2), as described in Table 2. Spectra for ν_e are shown as thick lines, while $\bar{\nu}_e$ are thin lines. The detectable part of the spectrum is shown with a light background. Relevant thermodynamic quantities are listed, with units as reported in Table 2.

between convective carbon burning and radiative carbon burning (Timmes et al. 1996; Heger et al. 2000; Hirschi et al. 2004).

Figure 2 shows the temperature–density profiles (i.e., the temperature as a function of the density) for each star model at the times t_n. The dashes/colors in the curves indicate which processes contribute most strongly to the total and partial emissivities, Q and $Q_{\rm th}$. As expected from prior literature (Itoh et al. 1996a), generally Q is mostly due to β processes at lower densities. Small islands of photoneutrino preponderance are observed at $\rho \sim 10^4$ g cm^{-3}, and pair production dominates for $\rho \gtrsim 10^6$ g cm^{-3} and $t \lesssim t_4$. At $t = t_5 = t_c$; an extended region of β dominance appears in the core, at $\rho \gtrsim 10^{7.5}$ g cm^{-3}. This phenomenon is consistent with the rapid increase in the rate of neutronization (electron capture) in the core as the onset of collapse approaches. Indeed, we find that at $t = t_5 = t_c$, electron capture is responsible for ∼99% of the total emissivity, Q, while the contribution of β decay is suppressed (only $\lesssim$1% contribution), as noted previously, in connection with the electron degeneracy.

Generally, the partial emissivity, $Q_{\rm th}$, follows the same trend as Q, with the major difference that β dominance is much more extended to high density, and islands of β-dominated emissivity are seen for ρY_e as high as $\rho Y_e \sim 10^7$ g cm^{-3}. In the core of the star, $Q_{\rm th}$ is always dominated by either pair neutrinos or β processes, with the same region of fast neutronization, as noted for Q.

Since submission of this work, Yoshida et al. (2016) has shown the time evolution of the neutrino signal from stars with initial masses of 12, 15, and 20 $M_\odot$ models, evolved up to core collapse. They find that pair production dominates over β processes up to a few hours before collapse, with β processes only becoming dominant a few seconds before collapse. Due to this dominance of pair neutrinos, Yoshida et al. (2016) focus only on that process in their study of spectra and detected events, while β interactions are included only in the calculation of total energy loss and abundance evolution of their models.

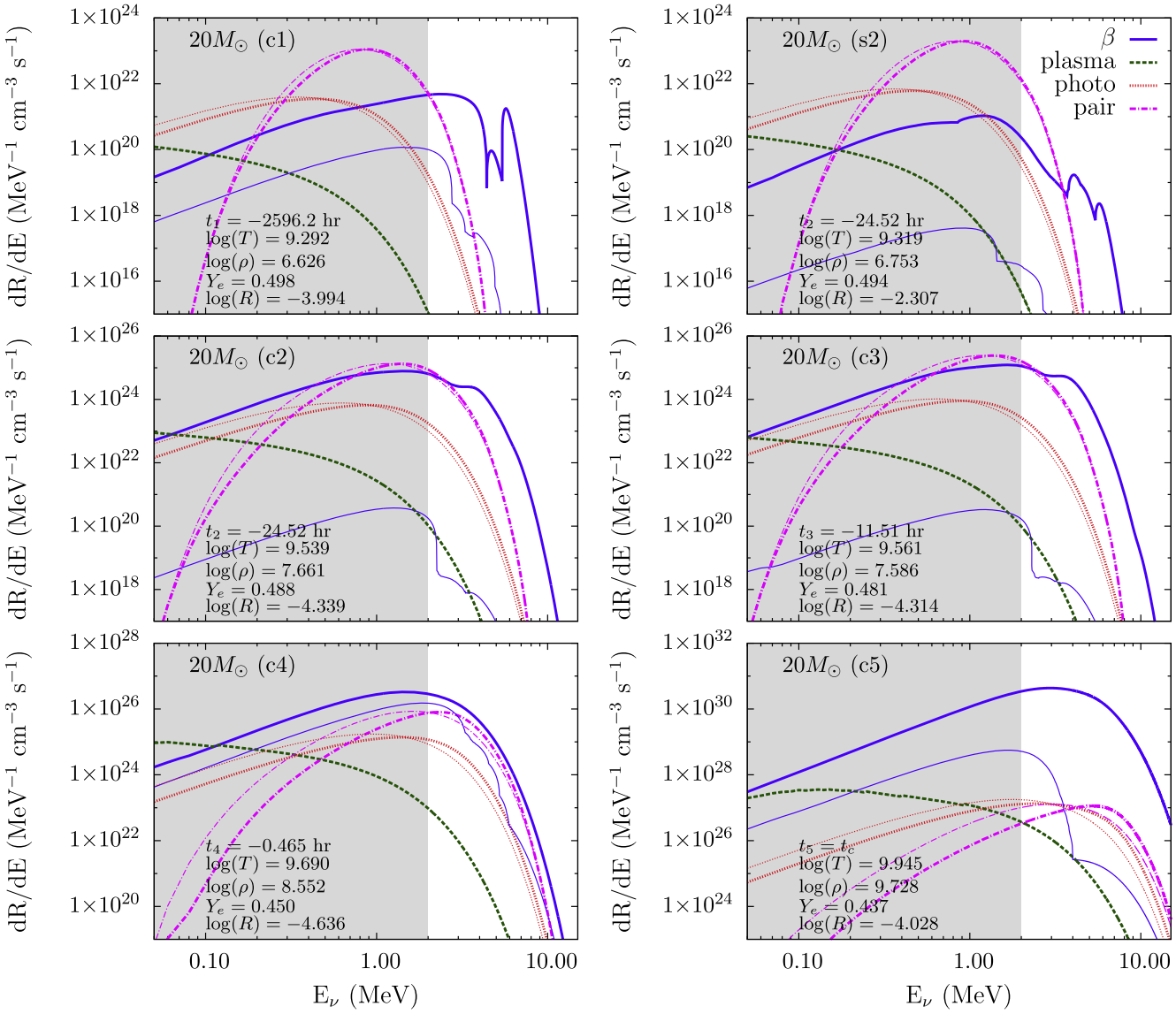

Figure 4. The same as Figure 3, for the points (c1)–(c5) and (s2), of the 20 $M_\odot$ star, as given in Table 2.

We find β decays to be comparable to pair production from ∼1 day before core collapse and dominant from ∼0.5 hr before collapse. As such, we include detailed calculations of the β spectrum, as well as thermal processes. Differences in the neutrino signal can be attributed to differences in the treatment of convection and convective overshooting, leading to differences in the core structure. The core masses in Yoshida et al. (2016) are larger than ours by ∼5%, an indication of a stronger convective overshoot treatment. For the 15 $M_\odot$ model, we found our core temperature and densities to be larger (∼30% and ∼70%, respectively). These higher temperatures will lead to an increase in the production of nuclei undergoing β processes, relative to that of Yoshida et al. (2016).

Summarizing, the results of this section suggest the importance of β processes for the detectable region of the parameter space—late times (where the neutrino luminosity is higher) and the highest energy part of the neutrino spectrum. The next section discusses neutrino energy spectra in more detail.

3.3. Spectra

We now illustrate the ν_e and $\bar{\nu}_e$ energy spectra for selected points inside the star at the times t_n. The details about them are given in Table 2. These points represent examples of cases when β processes contribute substantially to the neutrino spectrum in the detectable energy window. All points are at the center of the stellar core, except for point (s2), which is situated at the edge of the core at time t_2, the beginning of core silicon burning. In addition to the neutrino emissivities at these specific points, Table 2 also includes the values of the total emissivity integrated over the entire volume of the star, $Q_{\rm int}$, at the various times.

Figures 3–6 show the contribution of the different processes to the neutrino spectra for each progenitor model. We see that, despite the individual differences discussed in Section 3.2, the main features of the spectra are common to all the stellar models. Specifically, at points (c1) and (s2), pair production has the dominant contribution at $E \sim$ MeV, with plasma neutrinos and photoneutrinos becoming increasingly important,

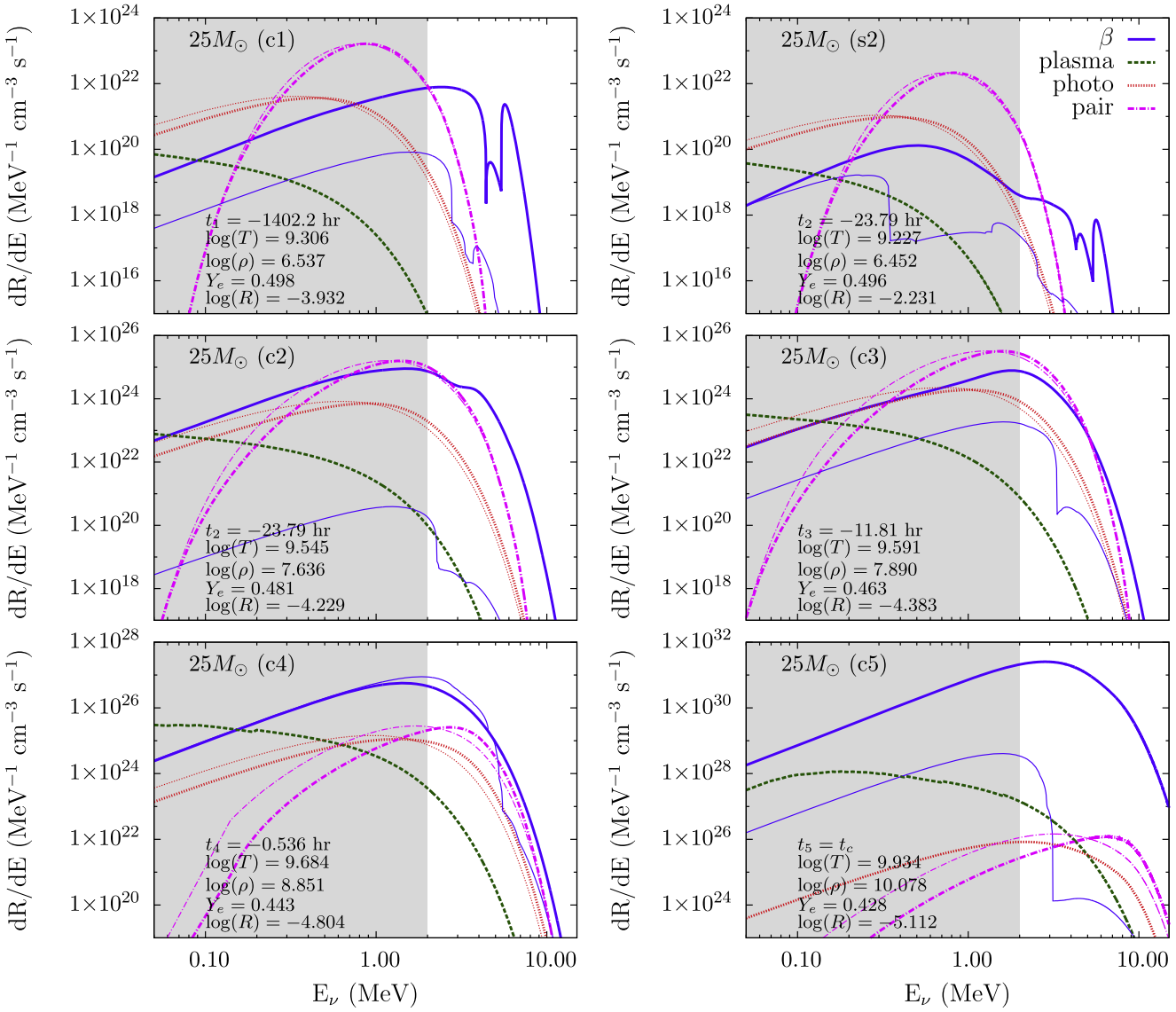

Figure 5. The same as Figure 3, for the points (c1)–(c5) and (s2), of the 25 $M_\odot$ star, as given in Table 2.

or even dominant, at lower energies. In the tail of the spectrum, $E \gtrsim E_{\rm th} = 2$ MeV, the major contributions to the energy spectrum are from pair production and β processes. The latter can dominate by several orders of magnitude at $E \sim$ 7–10 MeV, which is a realistic energy threshold for a Mt-mass water Cherenkov detector (Abe et al. 2011). In the core, the contribution of β processes to the spectrum is substantial at all energies for $t \gtrsim t_2$ (points (c2)–(c5)), and dominates by more than one order of magnitude at the onset of collapse (point (c5)). Generally, β processes contribute more strongly to the ν_e spectrum, due to the high rate of electron capture, but still they can play a major role for the $\bar{\nu}_e$ spectrum as well (for points (c4) and (c5), see, e.g., the bottom of Figures 3–6).

The structure of the β spectra in Figures 3–6 is as expected: one can identify the characteristic smooth shape of β decay spectra and, especially at lower temperatures (e.g., point (c1)), the peaks due to electron capture. At higher temperatures, these peaks are widened by thermal effects (see, e.g., Odrzywolek 2009) and ultimately form a continuum with one another and with the electron capture spectrum (points (c3), (c4), and (c5)).

We have identified the specific decays that produce the most prominent β peaks. For all progenitor models, at points (c1) and (s2), where the temperatures and densities are relatively low, the major contributors are isotopes around $A \approx 30$. In particular, the two peaks at high energy in the ν_e spectrum for the point (c1) in all stellar masses are produced by electron capture on ^{31}S and ^{30}P. The high energy peaks in the spectrum for point (s2) are due to electron capture on ^{30}P for 15 $M_\odot$; ^{31}P, ^{31}Si, and ^{48}V for 20 $M_\odot$; ^{31}Si and ^{31}S for 25 $M_\odot$; and ^{31}S for 30 $M_\odot$. The peaks in the $\bar{\nu}_e$ spectra are also due to sulfur, phosphorous, and silicon isotopes around $A \approx 30$. As the temperature and density increases, the isotopes dominating the β process spectrum move to higher A. The ν_e and $\bar{\nu}_e$ spectra for points (c3)–(c5) have the highest contributions from iron, cobalt, manganese, and chromium isotopes, as well as capture reactions on neutrons and protons. This is consistent with the findings of Odrzywolek (2009). The possibility that these decays might, at least in principle, be observed in a neutrino spectrum could serve as motivation for further theoretical study.

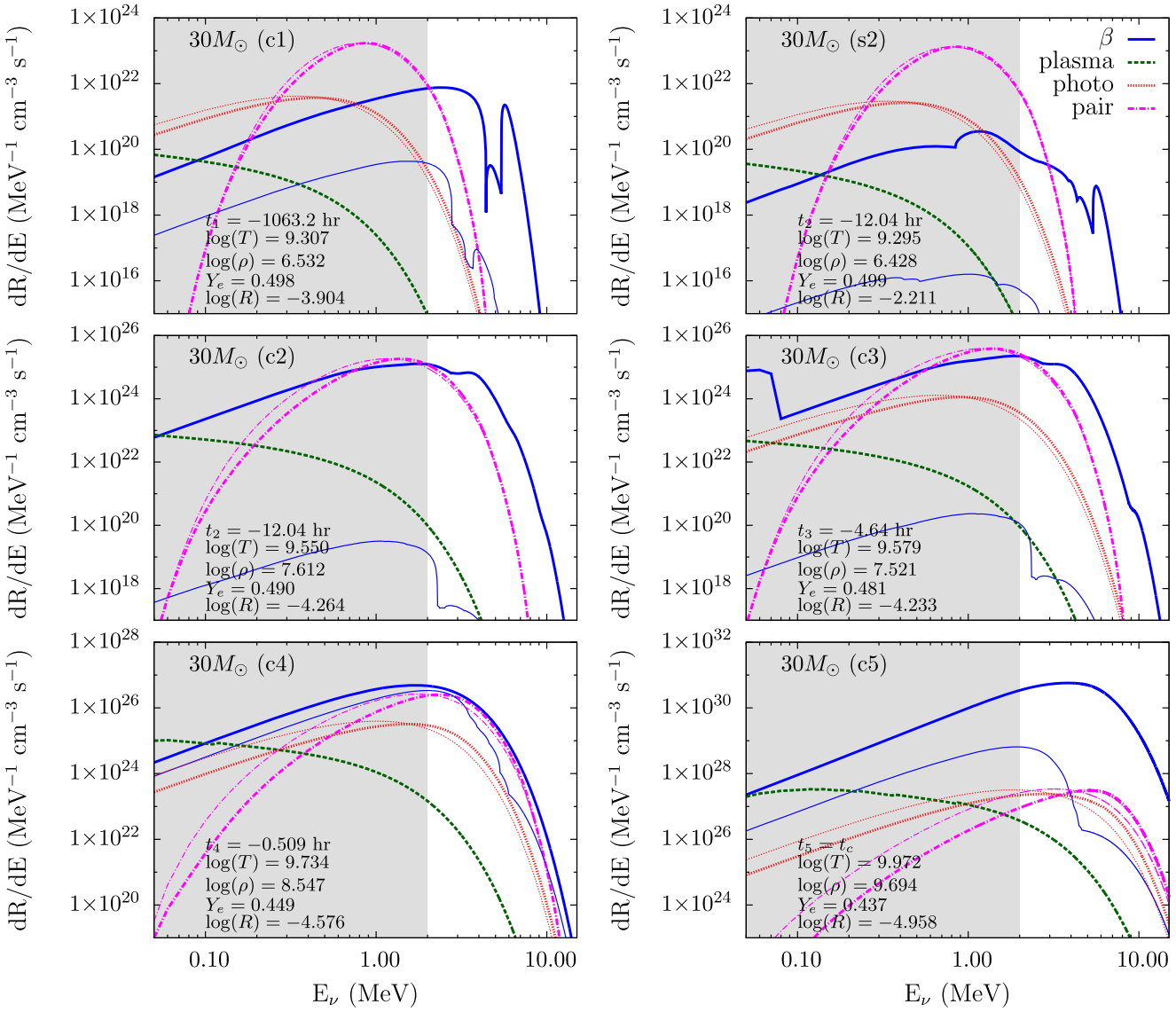

Figure 6. The same as Figure 3, for the points (c1)–(c5) and (s2), of the 30 $M_\odot$ star, as given in Table 2.

4. Summary and Discussion

We have performed a new study of the neutrino emission from a star in the presupernova phase. This work is the first to combine all the relevant microphysics—including β processes—with a state-of-the art numerical simulation of stellar evolution. We were able to obtain, for the first time, accurate and consistent neutrino fluxes and spectra from β processes, using the detailed isotopic composition calculated by the MESA code, with a nuclear network of up to 204 isotopes. The ν_e and $\bar{\nu}_e$ emissivities and spectra were calculated for selected times and locations inside the star, and for four stellar progenitors of different masses. Particular emphasis was placed on the detectable part of the spectrum, above an indicative threshold of 2 MeV.

It was found that, in part of the parameter space, β processes contribute substantially to the detectable neutrino flux, even when they are subdominant to the entire neutrino emissivity (integrated over the entire spectrum). In the last minutes before collapse, the ν_e flux from electron capture largely dominates—by more than one order of magnitude—the neutrino emission in the core of the star at energies relevant for detection. Some of the β decays that contribute the most, due to having high Q-value, were identified; they would be an interesting target of further study to obtain more reliable spectra above realistic detection thresholds.

Results for different stellar models show that the time evolution of the neutrino flux is strongly progenitor-dependent, reflecting the faster evolution of more massive stars through the different stages of nuclear burning (see, e.g., Paxton et al. 2011). Therefore the time distribution of a presupernova neutrino signal in a detector might be a new tool to learn about supernova progenitors. This could be especially interesting in the context of failed supernovae: the observation of neutrinos from advanced nuclear burning, combined with an anomalously short neutrino burst (truncated by the direct collapse into a black hole; see, e.g., Sumiyoshi et al. 2007), would unambiguously identify a failed supernova, and help constrain its progenitor mass. Such constraint would contribute to the debate on what characteristics of the progenitor star (mass, compactness, etc.) are most strongly correlated with direct black hole formation (see, e.g., O'Connor and Ott 2011; Pejcha & Thompson 2015).

We find that the ν_e and $\bar{\nu}_e$ fluxes should dominate over the ν_x ones. This could, in principle, make presupernova neutrinos a tool to test neutrino oscillations by looking for the permutation of energy spectra of the different flavors. Interestingly, the oscillation pattern might be different from that expected for the post-collapse flux. Specifically, the presupernova flux might be free from the still poorly understood collective oscillation effects—driven by neutrino–neutrino coherent scattering (see, e.g., Duan & Kneller 2009; Duan et al. 2010)—that are active when the number flux of neutrinos is high and the matter density profile is suppressed behind the launched shockwave (Hannestad et al. 2006; Mirizzi et al. 2016). Without the complication of collective effects, oscillations of presupernova neutrinos might offer a particularly clean test of the matter-driven flavor conversion (MSW effect; Wolfenstein 1978; Mikheev & Smirnov 1986a, 1986b).

A step forward toward a study of the detectability of presupernova neutrinos will be to integrate the emissivity over the whole star's core and inner shells, and for several time steps, so as to obtain the total neutrino flux, its spectrum, and its time evolution. This will be the subject of our future work.

We are deeply grateful to F. X. Timmes for very insightful comments and encouragement, and thank A. Odrzywolek for fruitful discussion. We are also indebted to the anonymous referee for stimulating feedback. K. M. Patton and C. Lunardini acknowledge the National Science Foundation grant number PHY-1205745, and the Department of Energy award DE-SC0015406. K. M. Patton also acknowledges the US Department of Energy grant DE-FG02-00ER41132. R. Farmer acknowledges support from NASA under the Theoretical and Computational Astrophysics Networks (TCAN) grant NNX14AB53G, and NSF under the Software Infrastructure for Sustained Innovation (SI^2) grant 1339600.

References

Abe, K., Abe, T., Aihara, H., et al. 2011, arXiv:1109.3262
Alekseev, E. N., Alekseeva, L. N., Volchenko, V. I., & Krivosheina, I. V. 1987, JETPL, 45, 589
An, F., An, G., An, Q., et al. 2016, JPhG, 43, 030401
Asakura, K., Gando, A., Gando, Y., et al. 2016, ApJ, 818, 91
Aufderheide, M. B., Fushiki, I., Fuller, G. M., & Weaver, T. A. 1994a, ApJ, 424, 257
Aufderheide, M. B., Fushiki, I., Woosley, S. E., & Hartmann, D. H. 1994b, ApJS, 91, 389
Bionta, R. M., Blewitt, G., Bratton, C. B., et al. 1987, PhRvL, 58, 1494
Bishai, M., McCluskey, E., Rubbia, A., & Thomson, M. 2015, Long-Baseline Neutrino Facility (LBNF) and Deep Underground Neutrino Experiment (DUNE) Conceptual Design Report, Vol. 1, Available at http://lbne2-docdb.fnal.gov/cgi-bin/ShowDocument?docid=10687
Braaten, E., & Segel, D. 1993, PhRvD, 48, 1478
Duan, H., Fuller, G. M., & Qian, Y.-Z. 2010, ARNPS, 60, 569
Duan, H., & Kneller, J. P. 2009, JPhG, G36, 113201
Dutta, S. I., Ratkovic, S., & Prakash, M. 2004, PhRvD, 69, 023005
Farmer, R., Fields, C. E., Petermann, I., et al. 2016, ApJS, 227, 22
Fuller, G. M., Fowler, W. A., & Newman, M. J. 1980, ApJS, 42, 447
Fuller, G. M., Fowler, W. A., & Newman, M. J. 1982a, ApJ, 252, 715
Fuller, G. M., Fowler, W. A., & Newman, M. J. 1982b, ApJS, 48, 279
Fuller, G. M., Fowler, W. A., & Newman, M. J. 1985, ApJ, 293, 1
Grevesse, N., & Sauval, A. J. 1998, SSRv, 85, 161
Hannestad, S., & Madsen, J. 1994, PhRvD, 52, 1762
Hannestad, S., Raffelt, G. G., Sigl, G., & Wong, Y. Y. Y. 2006, PhRvD, 74, 105010 (Erratum: PhRvD 76, 029901 (2007))
Heger, A., Langer, N., & Woosley, S. E. 2000, ApJ, 528, 368
Heger, A., Woosley, S. E., Martinez-Pinedo, G., & Langanke, K. 2001, ApJ, 560, 307
Hirata, K., Kajita, T., Koshiba, M., et al. 1987, PhRvL, 58, 1490
Hirschi, R., Meynet, G., & Maeder, A. 2004, A&A, 425, 649
Itoh, N., Adachi, T., Nakagawa, M., Kohyama, Y., & Munakata, H. 1989, ApJ, 339, 354
Itoh, N., Hayashi, H., Nishikawa, A., & Kohyama, Y. 1996a, ApJS, 102, 411
Itoh, N., & Kohyama, Y. 1983, ApJ, 275, 858
Itoh, N., Mutoh, H., Hikita, A., & Kohyama, Y. 1992, ApJ, 395, 622
Itoh, N., Nishikawa, A., & Kohyama, Y. 1996b, ApJ, 470, 1015
Kato, C., Azari, M. D., Yamada, S., et al. 2015, ApJ, arXiv:1506.02358
Kutschera, M., Odrzywolek, A., & Misiaszek, M. 2009, AcPPB, 40, 3063
Langanke, K., & Martinez-Pinedo, G. 2001, ADNDT, 79, 1
Langanke, K., Martinez-Pinedo, G., & Sampaio, J. M. 2001, PhRvC, 64, 055801
Martinez-Pinedo, G., Langanke, K., & Dean, D. J. 2000, ApJS, 126, 493
Mikheev, S. P., & Smirnov, A. Yu. 1986a, JETP, 91, 7
Mikheev, S. P., & Smirnov, A. Yu. 1986b, NCimC, 9, 17
Mirizzi, A., Tamborra, I., Janka, H.-T., et al. 2016, NCimR, 39, 1
Misiaszek, M., Odrzywolek, A., & Kutschera, M. 2006, PhRvD, 74, 043006
O'Connor, E., & Ott, C. D. 2011, ApJ, 730, 70
Oda, T., Hino, M., Muto, K., Takahara, M., & Sato, K. 1994, ADNDT, 56, 231
Odrzywolek, A. 2007, EPJC, 52, 425
Odrzywolek, A. 2009, PhRvC, 80, 045801
Odrzywolek, A., & Heger, A. 2010, AcPPB, 41, 1611
Odrzywolek, A., Misiaszek, M., & Kutschera, M. 2004a, APh, 21, 303
Odrzywolek, A., Misiaszek, M., & Kutschera, M. 2004b, AcPPB, 35, 1981
Paxton, B., Bildsten, L., Dotter, A., et al. 2011, ApJS, 192, 3
Paxton, B., Cantiello, M., Arras, P., et al. 2013, ApJS, 208, 4
Paxton, B., Marchant, P., Schwab, J., et al. 2015, ApJS, 220, 15 (Erratum: ApJS 223, 1 (2016))
Pejcha, O., & Thompson, T. A. 2015, ApJ, 801, 90
Ratkovic, S., Dutta, S. I., & Prakash, M. 2003, PhRvD, 67, 123002
Sullivan, C., O'Connor, E., Zeger, R. G. T., Grubb, T., & Austin, S. M. 2016, ApJ, 816, 44
Sumiyoshi, K., Yamada, S., & Suzuki, H. 2007, ApJ, 667, 382
Takahashi, K., Yoshida, T., & Umeda, H. 2013, ApJ, 771, 28
Timmes, F. X., Woosley, S. E., & Weaver, T. A. 1996, ApJ, 457, 834
Weaver, T. A., Zimmerman, G. B., & Woosley, S. E. 1978, ApJ, 225, 1021
Wolfenstein, L. 1978, PhRvD, 17, 2369
Woosley, S. E., Heger, A., & Weaver, T. A. 2002, RvMP, 74, 1015
Yoshida, T., Takahashi, K., Umeda, H., & Ishidoshiro, K. 2016, PhRvD, 93, 123012